Chapter 7

Some Other Topological Problems in Microscopic Pathology

In making microscopic diagnosis of various organ changes, we often face problems that will better be approached if we are equipped with knowledge about the ABC of topology. Already, topological way of thinking has been introduced in Chapters 5 and 6, in the former of which it was pointed out that in distinguishing among variously differentiated adenocarcinoma and adenoma, changes of glandular skeleton serve as equally important a clue as changes of individual cells. However, so long as 2-D sectional images are examined, changes of structure in this aspect only provide the observers with a vague sense of abnormality. Only when visualized in 3-D pictures, the abnomalities of carcinomatous glands were disclosed so clearly as to allow us to define in accurate geometric terms how and to what degree the glandular structure is deviated from the norm. The deviation proved to involve the inner connectivity of normally tree pattern: generation of redundant branches that creates a network, or partial loss of branches causing the network to crumble into parts.

There are also similar aspects in the interpretation of 2-D microscopic images, and here too, we are assisted by applying the topological way of thinking. This is because sometimes in a 2-D section of diseased organs, structural changes of non-metric character play an essential role in creating the picture. Again, such changes have nothing to do with the length, area, volume or angle, but are associated with features sustainable during continuous transformation, as the number of holes contained in a network. All these features belong to the aspect of morphology where one can measure the grade of deviation by applying topological parameters. Added in this chapter are some other examples of such problems.

a) Changes of pattern from chronic hepatitis to cirrhosis

Cirrhosis, chronic hepatitis and intermediate stage (Figs. 7-1, 7-2)

To be shown as the first example is the change of microscopic pattern from chronic hepatitis to cirrhosis. On what criteria do we differentiate between the two conditions microscopically? Nowhere we can draw a clear borderline. The whole process advances continuously, and we can only compare between arbitrarily chosen two livers and discuss, which of the two is more (or less) advanced. When we have a disease of an organ that shows a continuous transition of picture from one stage to another, its

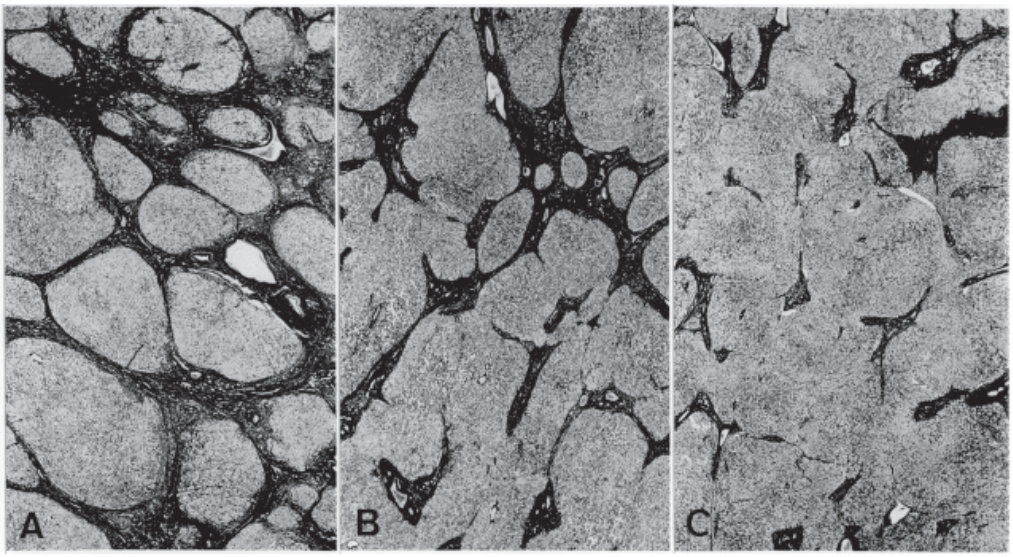

Fig. 7-1. Three different microscopic patterns of chronic liver diseases. A: advanced cirrhosis with completed nodulation. C: chronic hepatitis wherer nodules are not well separated. B: an intermediate pattern between A and C. Gomori's silver stain. Reproduced from Takahashi and Matsumoto: Tohoku J exp Med (1980), 131: pp. 322.

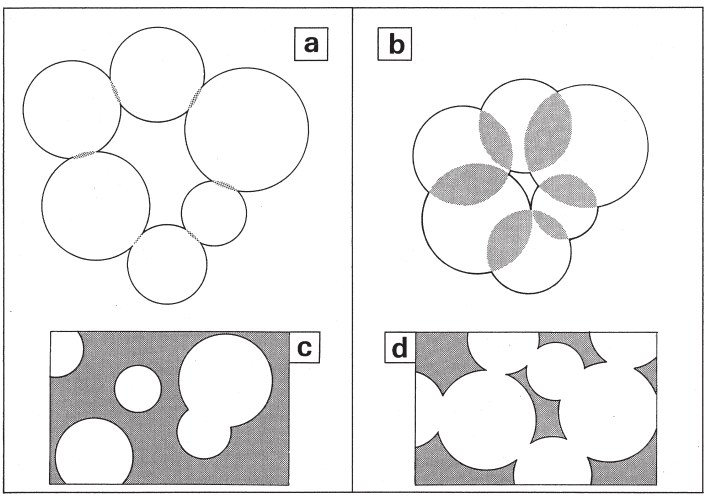

Fig. 7-2. Two-D topological difference between cirrhosis (c) and chronic hepatitis (d), related to their 3-D structure (a, b). Reproduced from Takahashi and Matsumoto: Tohoku J exp Med (1980) 131: pp. 315.

progression must be the very object to evaluate with a parameter, i.e., in terms of continuous quantity. Classification into separate groups is a time-honored method of study, that however works, strictly speaking, only when one can assume that the object comprises groups that in themselves are not continuous. To this problem, however, we will recur in the next chapter.

Now look at Fig. 7-1A. This is from an advanced cirrhosis where the microscopic section was silver-impregnated by Gomori method. One can find a typical two-phasic pattern, with the interstitial zones stained black and the regenerative nodules left unstained.

In Fig. 7-1C, a liver with chronic hepatitis is shown in order to compare with completed cirrhosis. In the parenchymal zone, there seems to be a tendency to swell with regeneration of hepatocytes, as shown by its partially rounded contour convex toward the interstitium. Still, the pattern of hepatic changes has yet to be qualified as cirrhosis, with quite incomplete nodulation. One can say at least that the pattern corresponds to a pre-cirrhotic condition, which cannot be expressed as real cirrhosis until necrotic foci have arisen one after another, adding to the preformed interstitial zone, and the parenchymal zone has undergone far more advanced nodular regeneration. The transition of pattern from chronic hepatitis to cirrhosis progresses along a continuous course, where morphologically no borderline exists separating the two conditions.

Then what is the difference in the above two patterns? By comparing the two, one may notice that it is the connectivity of the two phases that essentially differs. In cirrhosis (Fig. 7-1A), the interstitial phase is connected as a whole, separating the parenchymal zone into independent nodules. In contrast, we have a reversed state in chronic hepatitis of Fig. 7-1C, where it is the parenchymal zone that is connected over the entire picture, while the interstitial zone is split into separate parts.

There are of course a continuous series of intermediate stages. In the liver shown in Fig. 7-1B, both the parenchymal and the interstitial zones are halfway connected. Here the two phases seem to be embracing one another, forming an arabesque pattern. Pathologists may waver at this picture in deciding which diagnosis is more pertinent, chronic hepatitis or cirrhosis.

Three-dimensionally, as in Chapter 6, a liver with chronic hepatitis as well as cirrhosis has a parenchymal network as a common skeleton. Therefore the difference in 2-D pattern between the two conditions does not seem reflecting an essential difference in the skeleton. It appears that as in Fig. 7-2, the pattern of separate nodules in cirrhosis (c) is a 2-D section of nodules that in the three dimensions, are slightly connected (a). On the other hand, in chronic hepatitis the pattern of aggregated nodules (d) is likely to originate from a 3-D structure where the nodules are more deeply connected (b).

Various patterns related with angles subtended by interphasic curves (Fig. 7-3)

As above, a liver with chronic hepatitis passes through a continuous series of 2-D microscopic pictures as it advances toward the terminal stage of cirrhosis, and now we are dealing with a connectivity change in a two-phasic pattern, a process that consists in a gradual separation of nodules from initially connected parenchymal zone. In fact, pathological diagnosis of cirrhosis solely depends on the grade of nodular separation in microscopic pictures. In the following, let us consider how we can describe the degree of advancement toward cirrhosis, establishing an index of connectivity with which to describe different 2-D patterns (Takahashi and Matsumoto, 1980; Takahashi, 1982).

Connectivity in a 2-D, 2-phasic pattern can be translated to the curvature of linear interphasic boundaries, or interphases. In Figs. 7-3a and 7-3b, we assume that the non-

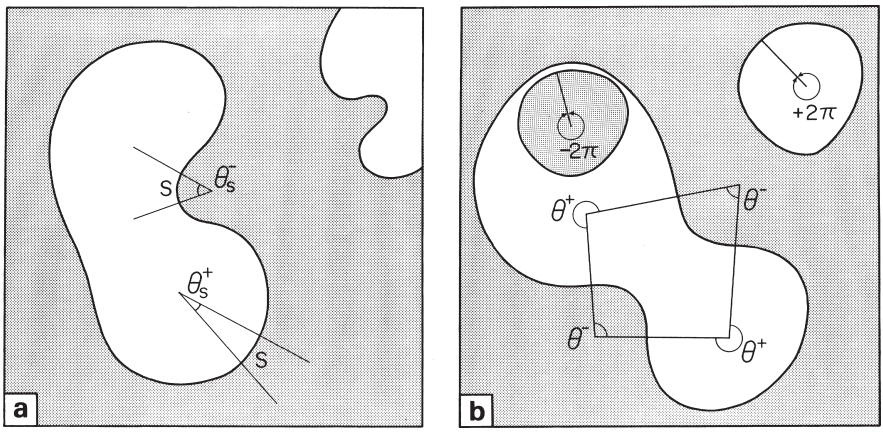

Fig. 7-3. **a**: definition of angle θ_s "subtended" by a minute segment S of interphasic boundary curve. The non-shaded areas are the parenchymal phase, the shaded the interstitial phase. θ_s is defined as a plus angle if the segment S is convex toward the interstitium; it is minus if S is concave. **b**: three different figures surrounded by a closed curve are correlated to the total angle subtended by the perimeter. For details see the text. Reprinted from Takahashi and Matsumoto: Tohoku J exp Med (1980) 131: pp. 315.

shaded areas are parenchymal, and the shaded areas are interstitial phase. Pay attention to the curves delimiting the two phases. In Fig. 7-3a, we take a minute segment S of curving interphase, and define the angle θ_s which is "subtended" by the segment. It corresponds to the angle between the normals drawn at the both ends of S. Here, plus and minus angles are to be distinguished according to whether, the interphase is convex or concave when viewed from the parenchymal phase. If S is convex toward the interstitium, θ_s shall be plus and denoted by θ_s^+, while it shall be minus (θ_s^-) if S is concave.

Now let us define θ_A, the total sum of angles in an area A, in two different forms. One is the absolute sum θ_A(abs), the sum of absolute values, in which we discard plus or minus. The other is the net sum θ_A(net), in which θ^- is added as minus angles. Accordingly,

$$\theta_A(\text{abs}) = \theta_A^+ + |\theta_A^-| = \theta_A^+ - \theta_A^-$$

and

$$\theta_A(\text{net}) = \theta_A^+ + \theta_A^-.$$

It may be clear from the definition of θ_A^+ and θ_A^- that $\theta_A(\text{abs}) \geqq 0$, and $\theta_A(\text{abs}) \geqq \theta_A(\text{net})$.

To what values θ(abs) as well as θ(net) amounts is to be shown in various examples. In Fig. 7-3b, there is a nodule in the right upper part, where the contour is entirely convex along the circumference, and here, both θ(abs) and θ(net) are $+2\pi$, because there is no minus angle. In a "lobulated" pattern in the middle of the figure where two nodules are connected, minus angles develop at the places of constriction. In this pattern, $\theta(\text{abs}) > 2\pi$ because lobulation generates redundant plus angles that

make the total θ^+ larger than $+2\pi$ and moreover there are minus angles that are added as absolute values. But θ(net) remains always $+2\pi$ in such an indented shape because the redundantly formed plus angles are exactly offset by the minus angles. Next, there is a hole in a nodule in the left upper part of the figure. If the interphase is concave toward the hole along the entire circumference, no plus angle exists. Therefore θ(abs) $= +2\pi$ and θ(net) $= -2\pi$.

The index of nodular separation ρ_θ (Fig. 7-4)

Based on the above, we define ρ_θ, the index of nodular separation, as

$$\rho_\theta = \theta_A(\text{net}) / \theta_A(\text{abs}). \tag{7-1}$$

One can see in Fig. 7-4 how ρ_θ describes a series of patterns that are different in terms of connectivity of the two phases. In the left upper figure (a) where all the nodules are round with the interphasic curve always convex toward the interstitium, $\rho_\theta = +1.0$, because θ(net) is $+2\pi$ for each nodule and equal to θ(abs). With beginning "lobulation" of nodules due to aggregation as in the right upper figure (b), $0 < \rho_\theta < +1.0$

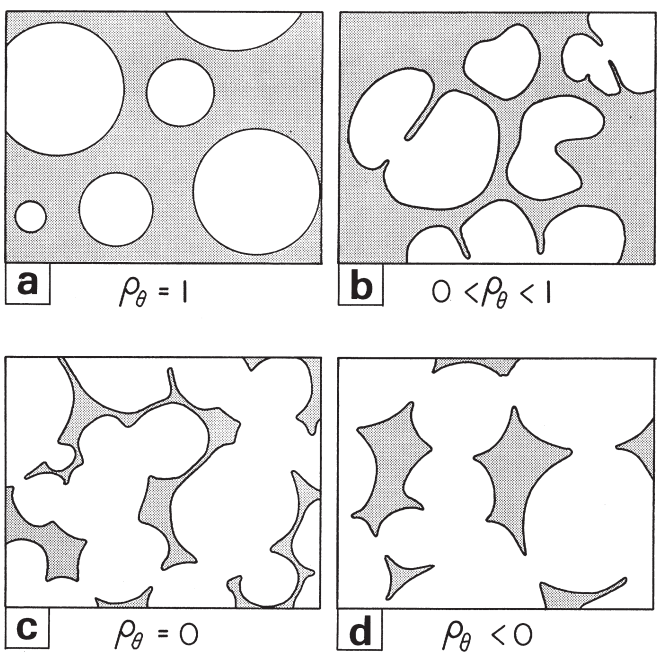

Fig. 7-4. Various patterns described with the index of nodular separation ρ_θ. When ρ_θ is +1.0 (upper left), the nodules are constantly convex toward the outside. As internodular connection begins (upper right), ρ_θ becomes smaller. When ρ_θ is 0, it describes an arabesque, where the parenchymal and interstitial phases embrace one another (lower left). A negative ρ_θ implies a reversed pattern (lower right) with the interstitial phase disconnected into separate parts. Reproduced from Takahashi and Matsumoto (1980): Tohoku J Exp Med 131, pp. 318.

because minus angles, developing at the places of constriction, make θ_A(abs) larger than θ_A(net). As aggregation advances, ρ_θ becomes smaller, and when it reaches 0, the pattern corresponds to "arabesque" as in the left lower figure (c), in which the two phases are embracing one another. If nodular connection advances further, we get a pattern of separate interstitium (d: right lower), or a reversed pattern, where $\rho_\theta < 0$.

Thus, the parameter describes a series of differently connected patterns as a continuous variable. If applied to liver diseases, the larger the value of ρ_θ, the more advanced the cirrhotic changes, and vice versa.

Determination of ρ_θ by tangent counting (Fig. 7-5)

ρ_θ is calculated by the equation (7-1), but how to estimate the total angles θ_A^+ and θ_A^- in an area A? These are obtained very easily by applying the tangent counting method proposed by DeHoff (1968, 1970). Consider, as in the upper part of Fig. 7-5, a rectangular area A which we assume to be sufficiently large and contain interphasic curves randomized with regard to their orientation. Let the shadowed area be the interstitial, and the non-shadowed area the nodular phase, respectively. Here we attempt to "sweep" the area with a line, for example the upper side of the rectangular, that is to be translated downward as the test line. With "sweeping," this line comes to contact at many places with the interphasic curves, generating tangents as denoted by symbols ○ and ×. It may be clear that the more meandering the curves, the larger the number T_A of tangents generated, which means, the more θ_A is contained in the area A.

Statistically, a tangent occurs at every π of angles "subtended" by the interphasic curves, if the area A is sufficiently large and the curves are randomized in their orientation. This would be understood intuitively as follows. We assume, as in the lower part of Fig. 7-5, that the linear interphasic boundaries in A are entirely split into a large number of sufficiently minute, elementary arcs, each of which subtends a minute angle $d\theta$. Let us pay attention to an elementary arc and consider the expected number dT of tangents that occur at the arc (of interest) when the area A is swept by a test line. Suppose that all $d\theta_s$ in A, together with the arcs, are collected by parallel translation to a point as in the right part of the figure. Then we can see a circle having an angle of 2π may be formed many times. Because sweeping generates a tangent at every hemicycle (π), the probability that it occurs at the arc (of interest) subtending $d\theta$ is $d\theta/\pi$. Accordingly, if the total expected number of tangents in A is T_A,

$$T_A = \int_A dT = \frac{1}{\pi}\int_A d\theta = \frac{1}{\pi}\theta_A(abs),$$

and we obtain

$$\theta_A(\text{abs}) = \pi \cdot T_A .$$

An accurate mathematical derivation will be found in the literature (DeHoff, 1968; Takaki and Arai, 1993). The estimate of θ_A^+ and that of θ_A^- are obtained by distinguishing between the tangents generated at convex (○) and concave parts (×) of curves. If the tangent number at convex and concave curves are denoted as T_A^+ and T_A^-, respectively,

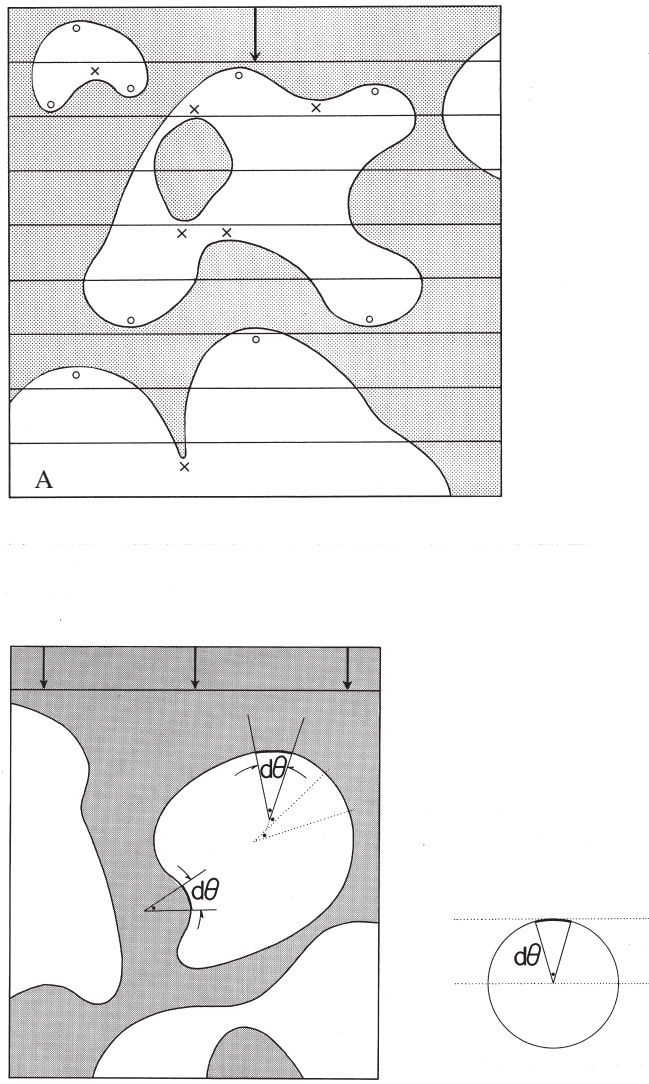

Fig. 7-5. Measurement by tangent counting of θ_A, the total angles subtended by the curving interphasic borders in an area A. For explanation see the text. Reproduced from Takahashi and Matsumoto: Tohoku J exp Med (1980), 131: pp. 319 and 321.

$$\theta_{A^+} = \pi \cdot T_{A^+}$$

and

$$\theta_{A^-} = -\pi \cdot T_{A^-}.$$

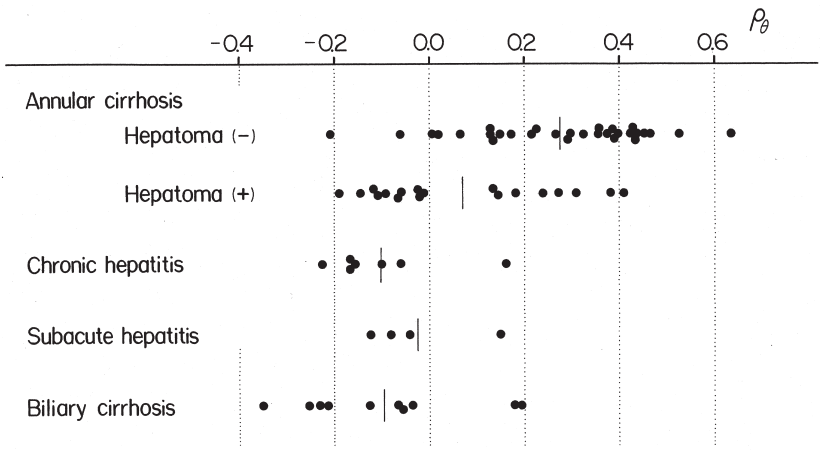

Fig. 7-6. Index of nodular separation ρ_θ estimated in various liver diseases. Reproduced from Takahashi and Matsumoto: Tohoku J exp Med (1980), 131: pp. 323.

ρ_θ estimated in various liver diseases (Fig. 7-6)

ρ_θ was obtained by measurement on seventy autopsy livers with different types of chronic diseases, including cirrhosis with or without hepatoma (hepatocellular carcinoma), chronic hepatitis, subacute hepatits and biliary cirrhosis (Fig. 7-6). These diagnoses were given microscopically by a number of pathologists in advance of morphometry. In cirrhosis, the obtained values of ρ_θ range from –0.21 to +0.64. That even the highest value is far lower than +1.0 may be understood by taking into account the 3-D structure of cirrhosis where the nodules are mutually joined to form chains (see Figs. 6-4, 6-5 and 6-9), producing indented contour of nodules. Cirrhoses were divided according to whether or not harboring hepatoma. In the group with hepatoma the mean ρ_θ is +0.07, a value much lower than +0.27 in the group without hepatoma, and the difference is significant at $p < 0.01$. Thus, seemingly less completed cirrhosis is likely to be rather more prone to cancer development. The mean ρ_θ was negative in all the remaining groups; –0.102 in chronic hepatitis, –0.023 in subacute hepatitis and –0.095 in biliary cirrhosis.

b) Two types of glandular tumors: papillary and tubular

Intraductal papilloma of breast: papillary and tubular types (Figs. 7-7, 7-8)

The glandular epithelium is a generic term for the epithelium that consists of glandular or secreting cells. If we introduce a term “glandular tumors” to express tumors developing from glandular epithelia, it includes a wide range of various tumors like adenoma, papilloma, adenocarcinoma and so on, totaling in frequency up to the largest share of tumors pathologists encounter in their routine diagnostic practice. Looking through the various pictures of glandular tumors, one may notice that there are basically two types, i.e., “tubular” and “papillary” types.

Figures 7-7 and 7-8 present typical microscopic pictures. These are tumors of the

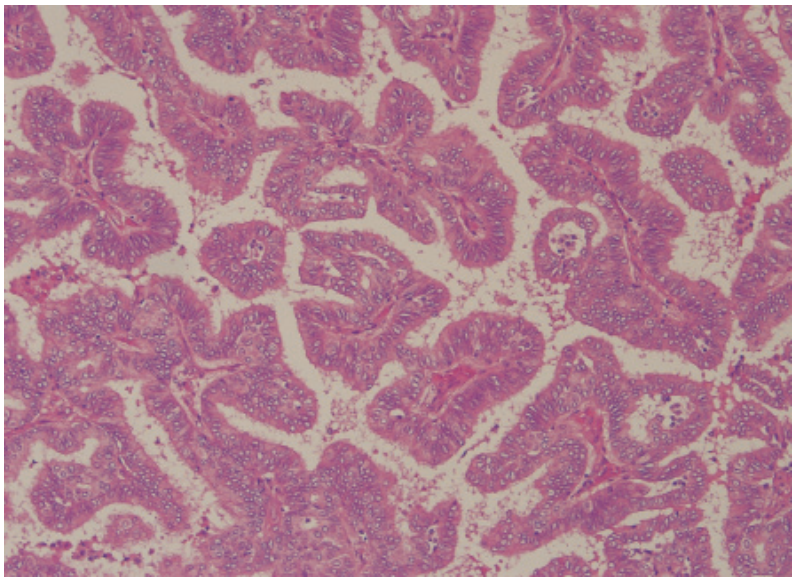

Fig. 7-7. Intraductal papilloma of the breast: papillary pattern. The tumor consists of finger-like rods, all having fibrovascular stroma and covered by a monolayer of epithelial tumor cells. Extending around the tumor cells is the void space, into which the glandular epithelia secrete their products. Hematoxylin-eosin stain.

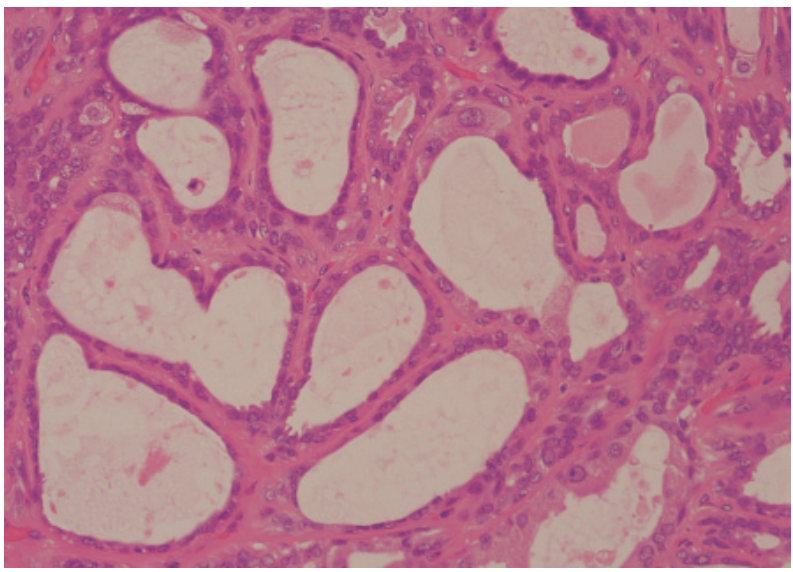

Fig. 7-8. Intraductal papilloma: tubular pattern. Here one can find multiple tubes that penetrate the stromal phase. The inner surface of the tubes is covered by tumor cells. The products of tumor cells are secreted into the lumina of tubes which in this pattern are the phase of void. Hematoxylin-eosin stain.

breast, both designated as intraductal papilloma, about which we already discussed in Chapter 4. In Fig. 7-7, the tumor appears consisting of numerous finger-like rods, each having a stroma made of connective tissue which is covered by epithelial tumor cells, presenting a form that may adequately be called a papillary tumor.

In Fig. 7-8, however, one can find a different pattern. Formed here are multiple tubes. They are separated by connective tissue stroma, and the neoplastic glandular cells are extending so as to cover the inner surface of the tubes, a pattern that can be expressed as a tubular tumor. Although conventionally diagnosed as intraductal papilloma, this type of tumor seems to be found not infrequently on microscopic examination of intraductal tumors of the breast. There are also intermediate tumors in which papillary and tubular patterns co-exist in various proportion. Thus, we find here a lesion which can present a series of different patterns between the two extremes. As to be shown, these varying patterns can exactly be defined from a connectivity point of view.

Topological difference between papillary and tubular patterns (Fig. 7-9)

Here again, we face the same problem as we saw in the foregoing section. Figure 7-9 is a schema explaining in what aspect the two patterns differ. Both papillary and tubular tumors consist of two phases, the stroma (shaded in the figure; one may also call interstitium) and the void (non-shaded). The proliferating tumor cells are lining along the interphasic border, while both of the phases are not in themselves a tumor. The stroma is an indispensable component of tumor because it contains blood vessels feeding the growing tumor cells. The void corresponds to the exterior spaces where products secreted by the tumor cells flow in, stay and are carried through.

Now, let us examine the connecting relation of the two phases. First we realize

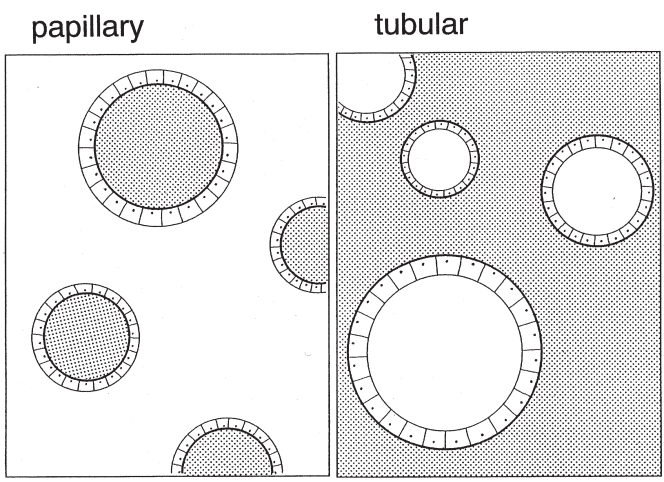

Fig. 7-9. Papillary vs. tubular tumors: their topological difference. In the papillary tumor (left), the void phase (non-shaded) is connected, separating the stromal phase (shaded) into pieces. The tubular tumor (right) corresponds to the reversed state, where the stromal phase is totally connected, disuniting the void phase. Thus the difference underlying the two patterns is reduced to that of topology.

that in the papillary tumor, the void phase is connected as a whole, separating the stromal phase into many pieces. In contrast, in the tubular tumor the connecting relation is reversed: the stroma is totally connected, and inevitably the void is disconnected into separate tunnels. Thus we understand that the difference between the two patterns is defined by connectivity, i.e., which of the two phases is connected, containing the other.

The situation is quite the same as what we saw in the livers with chronic hepatitis and those with cirrhosis. Consequently, also in the intraductal tumors of breast, we can apply the quantitative expression with ρ_θ to measure the degree to which a given tumor is papillary or tubular. This will help us correlate the grade of "papillarity" or "tubularity" with clinical or biological features of glandular tumors. Recently, Sasaki *et al*. attempted to evaluate the pattern of intraductal papillomas with ρ_θ by micromorphometry on surgically excised breast from 40 patients.

Morphometry of intraductal papillomas (Fig. 7-10)

Morphometry was performed on silver-impregnated sections. Figure 7-10 is an example of tubular tumor where the interstitial phase, comprising collagen, is stained black. As the interphasic border, we defined the basement membranes of the proliferating glandular cells, disregarding the tumor cells which were included in the void. Measurement was made with a microscope equipped with tessellated eyepiece of grid-type as entered in the figure, where the parallel transverse lines allowed the observer to find the places where a tangent with basement membranes would occur. Using the grid, point counting was performed at the same time to estimate the volume density of the stromal phase $V_v(s)$, as illustrated in Chapter 2 (Figs. 2-1, 2-2, 2-3).

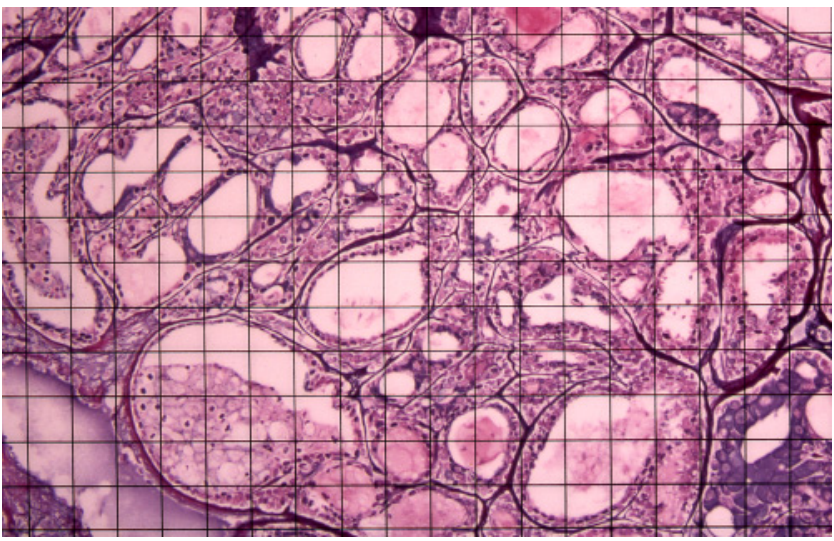

Fig. 7-10. Microscopic tangent counting for the pattern analysis of intraductal papilloma. The places where a tangent occurs between the interphasic border and the transverse parallel lines, are detected as the picture is slowly moved in the direction vertical to the lines. V_V(s), the volume density of stroma, can simultaneously be estimated by point counting. Gomori's silver stain.

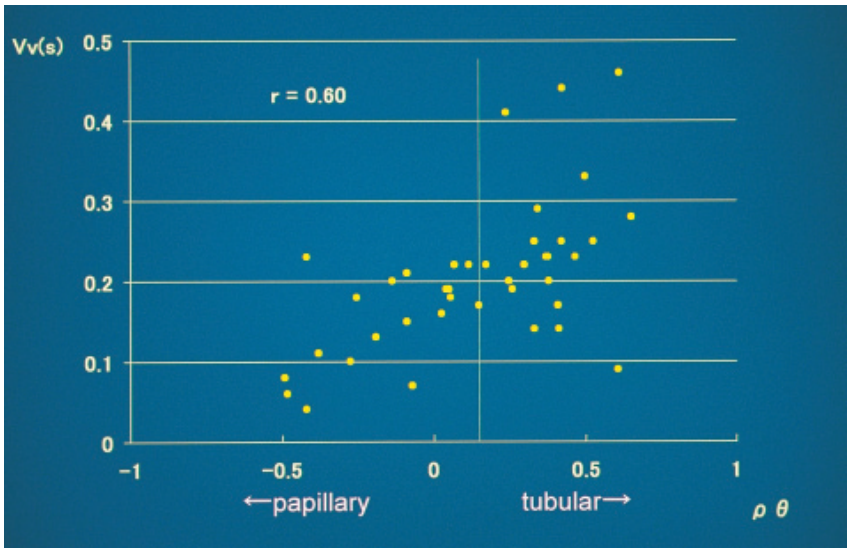

Fig. 7-11. Index of tubularity ρ_θ estimated in 40 intraductal papillomas. ρ_θ is presented in the abscissa, and V_V(s) in the ordinate. The mean ρ_θ is +0.14, showing that in the microscopic pictures, tubular pattern dominates over papillary, betraying the term "papilloma." Interestingly, there is a significant correlation between ρ_θ and V_V(s), showing that the more tubular the tumor, the more stromal component it contains.

Obtained values of ρ_θ and its correlation with $V_v(s)$ (Fig. 7-11)

Figure 7-11 presents the result of measurement, with ρ_θ in the abscissa and $V_v(s)$ in the ordinate. This time, ρ_θ was defined as an index of tubularity: the larger the value, the more tubular the pattern, and the smaller, the more papillary. When $\rho_\theta = 0$, the pattern consists of a mixture with tubular and papillary components, each having an equal share. As shown, ρ_θ ranges from –0.5 to +0.7, with a mean of +0.14. A mean value that proved to be plus demonstrates that in intraductal papilloma as a whole, tubular pattern predominates over papillary. Therefore, strictly speaking, "intraductal tubular adenoma" may be a more appropriate term than intraductal papilloma.

There is another finding which is more intriguing. One can see a positive correlation between ρ_θ and $V_v(s)$, the volume density of the stromal zone. The correlation coefficient, calculated at +0.60, is significant at $p < 0.01$. It demonstrates that, of the intraductal tumors of the breast, the more tubular the pattern, the larger the volume ratio of stroma contained in the tumor, and *vice versa*. We think this is a result quite significant in studying the morphogenetic difference between the two types of glandular tumors.

Morphogenesis for tubular and papillary tumors (Figs. 7-12, 7-13)

Figure 7-12 is a schema illustrating an assumption on the morphogenesis of tubular and papillary tumors. The figure in the upper part means a normal mucosa of mammary duct where a monolayer of epithelial cells are lining along the surface. The cells are laid on a basement membrane covering the stroma (shaded), the connective tissue that lies beneath and holds the membrane. The right lower figure expresses a

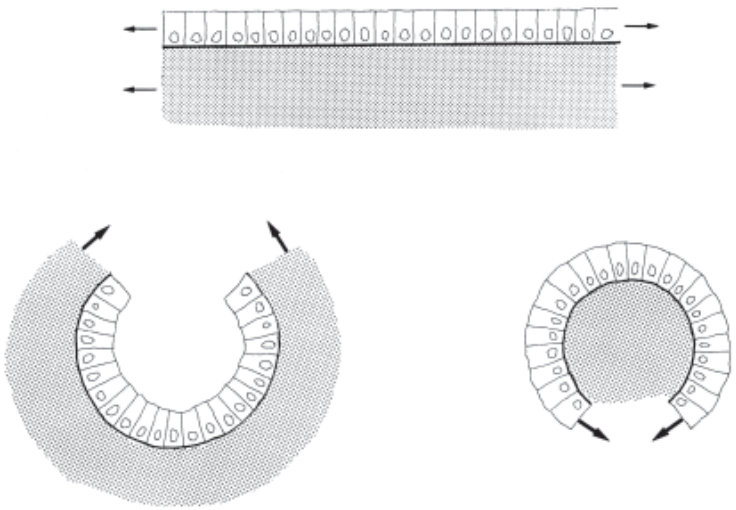

Fig. 7-12. A schema of morphogenetic difference betwen tubular and papillary tumors. For explanation see the text.

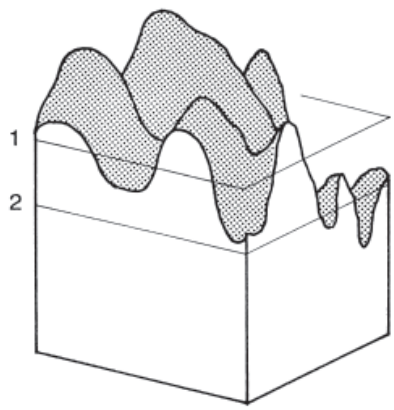

Fig. 7-13. Papillary and tubular tumors: difference in their 3-D structures. Consider that the cubic space contains an interphasic basement membrane covering the stromal phase that is under the mambrane. The upper part of the space corresponds to the void. The membrane forms several mountains and depressions, and if the cube is cut at Level 1, a papillary pattern emerges in the section, while at Level 2, a tubular pattern will be produced.

papillary tumor. Here the epithelial tumor cells, proliferating so as to extend the epithelial surface, grow faster than the connective tissue of stroma, and as the result, the stroma gradually comes to be wrapped by the superficial tumor cells, resulting in the formation of papilloma pattern. Quite the opposite is found in the morphogenesis of tubular tumor, as in the left lower. In this tumor, the stroma grows at a speed higher

than the epithelial tumor cells, and this makes the void phase being contained by faster-growing stromal phase. The result will be the formation of tubular tunnels.

It is often said that with regard to the morphogenesis of various tumors, it is the stromal tissue rather than the tumor cells themselves that determines the form (Sakakura *et al*., 1976). The present study seems to be giving a support to this concept.

In the above, the difference between papillary and tubular tumors has been discussed solely on 2-D sectional pictures. Then, what difference is there in the 3-D? Figure 7-13 is a schema correlating the 2-D patterns with the corresponding 3-D structure. Imagine a form like geographical configuration which is meant to express the basement membrane of glandular tumor. We assume that the membrane is covering the stroma that lies beneath. Now one can see the membrane is elevated at several places and is depressed between the neighboring mountains. Suppose that this configuration is sectioned with a plane parallel to the ceiling. At Level 1, several sections of mountains appear in the 2-D picture creating a papillary pattern, while at Level 2, the ground depressions emerge as cavities, and this is equivalent to a tubular pattern. After all, no critical point seems to exist in the 3-D structure corresponding to the transition of connectivity in a 2-D section where the value of ρ_θ changes plus and minus.

c) Hepatocellular carcinoma: cord and plate types

Normal hepatocytes and sinusoids (Fig. 7-14)

As another example, the microscopic feature of hepatocellular tumor is to be

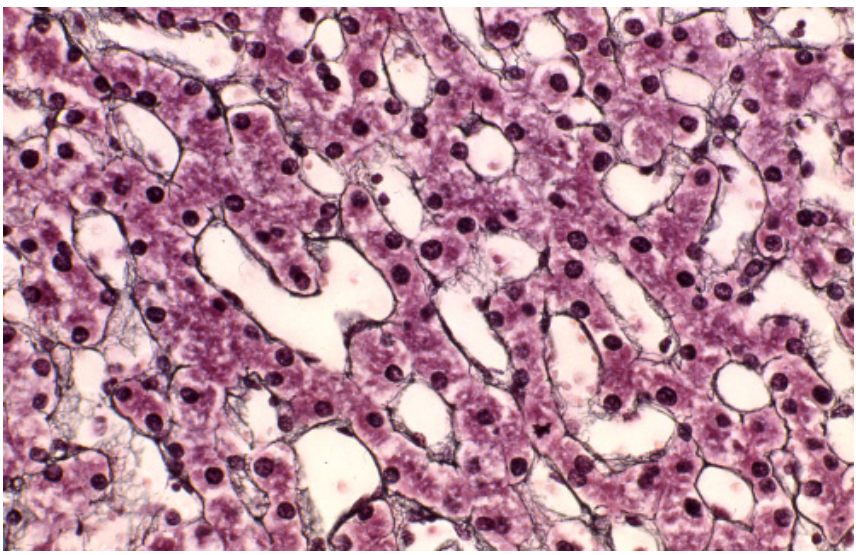

Fig. 7-14. Microscopic appearance of normal liver parenchyma. The hepatocytes seem forming continuous cords one cell breadth. The void spaces surrounded by the cords are the capillalries (sinusoids). Note that the hepatocytes are continuous throughout the picture, while the sinusoids are all split apart by hepatocytes, presenting a topological question of form. Gomori's silver stain.

added as a case for the application of ρ_θ. In Fig. 7-14 we revisit the normal intralobular parenchyma of the human liver (also see Figs. 3-26 and 3-27). The section is silver impregnated, with the hepatocytes stained wine red, their basement membranes black, and the capillaries (sinusoids) left as void spaces. Here again we find in the hepatic parenchyma a two-phasic structure comprising hepatocytes and capillaries, with the basement membrane delimiting the two phases. Now let us consider what a basic 3-D structure the hepatocytes are forming. The cells seem arranged in the form of continuous rows one-cell thick. Previously, an expression "liver cell cord" had been coined to describe this arrangement of hepatocytes. Though used for a long time, this term was abandoned after Elias (1949) pointed out its inadequacy from a structural viewpoint. Pay attention to the connecting relation between the two phases, and it may be clear that the capillaries are all separated into pieces, while on the other hand, hepatocytes are all connected over the whole picture, forming a continuum. Then what a 3-D structure should be assumed for each of them? It may be understood that the capillaries that are not united in a 2-D section, if integrated into 3-D by reconstruction from serial sections, will certainly present a linear structure, or in other words, a system of cords. However, the hepatocytes that are all continuous in a section cannot be a cord in the 3-D. Instead, they make plates, or "muralium," to use an expression by Elias. Though having curved surfaces and finely anastomosed, the aggregates of hepatocytes are certainly a plate facing the sinusoids with both of the sides, so long as a small part of the aggregate is concerned. Today, hepatocytes are correctly said to form "liver cell plates."

Hepatocellular carcinoma: plate and cord types (Fig. 7-15)

Figure 7-15 presents two microscopic types of hepatocellular carcinoma. These are from the study of M. Nakamura *et al*. (1996) who noticed that there are a variety of

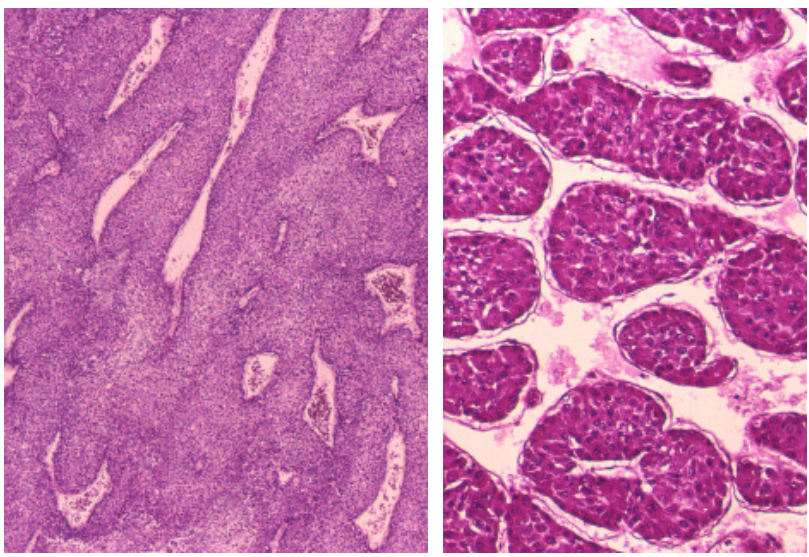

Fig. 7-15. Two patterns of hepatocellular carcinoma: the plate pattern (left) and the cord pattern (right).

tumors ranging over such a difference in the microstructural pattern. In the left, the carcinoma cells are forming plates. Although cells making up the tumor are stacked into a multilayer, the basic relation of the cell masses with the blood spaces is quite the same as in normal hepatic parenchyma. We call this the plate type tumor.

In the right, we can find a reversed pattern which corresponds to the papillary type of intraductal breast tumor. This may be called the cord type tumor. What we actually experience in most hepatocellular carcinomas is a mixture where the two patterns are co-existing in a tumor in various proportion. For some unknown reason, these two types have been described commonly as "trabecular type" in conventional classifications of hepatocellular carcinoma despite their apparently different patterns. It may be clear that one can apply without any modification the above quantification to these hepatocellular tumors.

d) The pattern of zonal hepatocellular necrosis: Is the acinar theory tenable?

It was shown in the above examples that in 2-D, 2-phasic patterns, there is an aspect in which the connectivity of phases plays a decisive role in the characterization of pattern. The different connectivity was measurable by "sweeping" the pictures with a test line where the number of tangents gave the estimates of total angles "subtended" by the interphasic border curves contained in an area, which then were correlated with the connectivity of phases. In reality, this methodology can be extended to the 3-D as proposed by DeHoff (1968). In this section, we show an application of this technique to the pattern analysis of zonal hepatocellular necrosis of the liver. The aim of this study is to examine whether or not the acinar theory of Rappaport is tenable, baed on the shape and distribution of necrosis. The following is the summary of an attempt performed by Y. Nakamura and Takahashi (1996, 1998).

Centrilobular necrosis in acute intoxication and chronic ischemia (Figs. 7-16, 7-17)

The zonal necrosis of the liver implies a confluent injury of hepatocytes involving a certain anatomical zone. For example, sometimes at autopsy, we find in the liver a necrosis of hepatocytes extending in the centrilobular zone or Zone 3 of Rappaport's acinus, although it remains a matter of question whether both of the zones are identical. Look at Fig. 7-16. This is a microphotograph of the autopsy liver from a patient dying of acute cresol intoxication on the third day. There are areas of coagulation necrosis (deeply stained), and clearly, these have a central vein at the center (C). On the other hand, there are areas in which hepatocytes are sustained without signs of necrosis, and these areas are connected as a whole, having portal tracts along the axis. On this pattern, it may be reasonable to say that this is a centrilobular necrosis.

Figure 7-17 presents another liver with centrilobular necrosis. This is from a patient who died of chronic cardiac failure due to aortic insufficiency. In this case there are necrotic areas, faintly stained but strongly congested, and their distribution seems to be essentially the same as in the foregoing case, having central veins along the congested axis (C). There is however a difference; the zone of parenchyma exempted from necrosis tends to have a rounded contour convex toward the necrotic

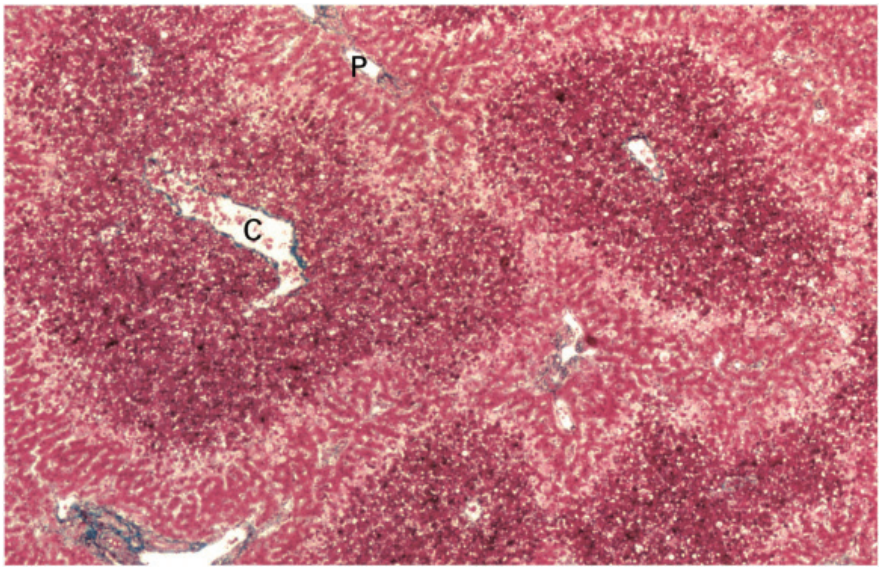

Fig. 7-16. Necrosis of liver from a patient dying in an acute stage of cresol intoxication. The hepatocytes in the central zone of lobules are uniformly destroyed as evidenced by the presence of central vein (C), the terminal hepatic venule, that is found at the center of necrotic area. The problem is whether, in geometric terms, the necrotic area sufficiently coincides with the form of what was defined as Zone 3 of Rappaport's acinus. Elastica-Goldner stain.

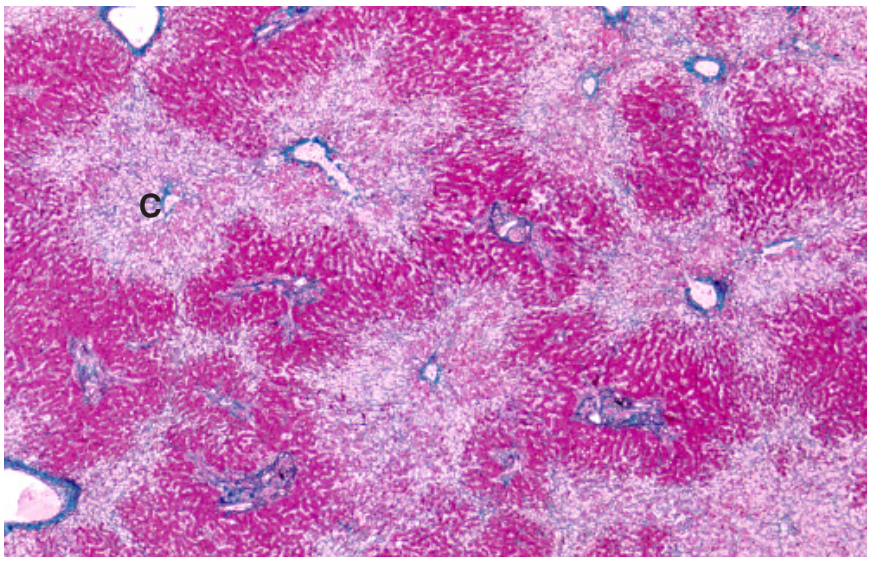

Fig. 7-17. Microscopic appearance of the liver in a patient who died of chronic congestive heart failure. Here too, necrosis is confined to the zone around the central vein (C). However, the shape of the necrotic areas is different from the cresol case, with the surviving parenchyma having a rounded contour because of nodular hepatocellular regeneration. Mallory's stain.

zone, perhaps because of nodular hepatocellular regeneration progressing during the long course of disease, for a matter of years. Here too, the areas that have survived are continuous, with terminal portal tracts positioned along their axis. In a patient in whom the liver has undergone severe ischemia but only for a terminal short period, the pattern of necrosis is quite the same as in the cresol cases.

The acinar model (Fig. 7-18)

The acinar model of Rappaport, illustrated in Chapter 3 (Fig. 3-6), is to be briefly revisited, because it is the very pathogenesis of zonal hepatic necrosis due to intoxication or ischemia that this hypothesis was proposed to explain. Using the schema of Fig. 7-18, Rappaport maintained that the structural unit of the liver must be defined as what he called acinus, a clump of parenchyma centered with a terminal portal venule and flanked by terminal hepatic venules (THV; synonymous to the central veins). The model is so illustrated that an acinus may comprise three zones, Zones 1, 2 and 3, which Rappaport says are arranged in the order of blood irrigation from the periportal to areas around the THV. Thus, Zone 3 (painted in pink) is assigned a position least advantageous from a sustenance of hepatocytes point of view, irrigated with blood delivering the lowest density of oxygen and nutrients that were already consumed in Zones 1 and 2. Hence, hepatocytes in Zone 3 are said to be the most liable to necrosis, in case of ischemia as well as intoxication. The problem with this theory is that with regard to the distribution, Zone 3 was defined so that it may extend from around the

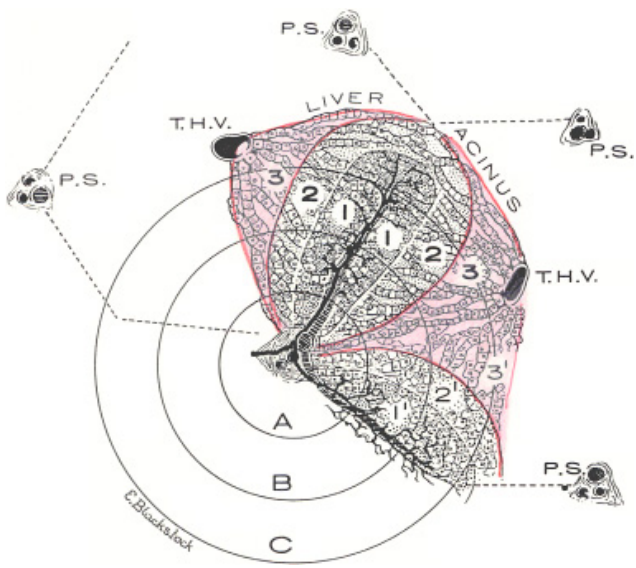

Fig. 7-18. The schema of an acinus given by Rappaport. The acinus is defined as a parenchymal clump that has a terminal portal venule at the center and is flanked by terminal hepatic venules (central veins). The parenchyma in an acinus is divided into Zones 1, 2 and 3. Of these, the hepatocytes in Zone 3 (pink), situated farthest apart from the afferent portal venule and consequently, are said to be most vulnerable to toxic or ischemic injuries. Reproduced from Rappaport *et al*. (1954): Anat Rec 119, pp. 11.

THV toward the portal tract in a "sleeve-like" fashion and reach the place where the three terminal portal venules come to join. This setting, particularly the assumption of "sleeves," seems to have been necessary in devising this model because otherwise, an acinus would not be separable even in a liver with Zone 3 necrosis, making it impossible to define the acinus as an independent unit. Accordingly, what we have to do is to examine in livers with acute and uncomplicated zonal necrosis whether or not an acinus discloses itself as a parenchymal clump independent from the neighboring ones. If it really does, then inevitably it ensues from the model that each of the non-necrotic part of acini, Zones 1 and 2, be demarcated from the necrotic Zone 3 with a plane that is convex toward the exterior over the entire surface.

In the hepatic lesions shown in Figs. 7-16 and 7-17 we have a 2-phasic structure: the phase of necrosis and that of parenchyma that has survived. In the following, let us consider how we can examine the geometric nature of the curved interfaces extending between the two areas.

The three types of surfaces (Fig. 7-19)

In solid geometry, surfaces are classified into three types: convex, concave and saddle, as in the lower part of Fig. 7-19. In case of zonal hepatic necrosis, let us take

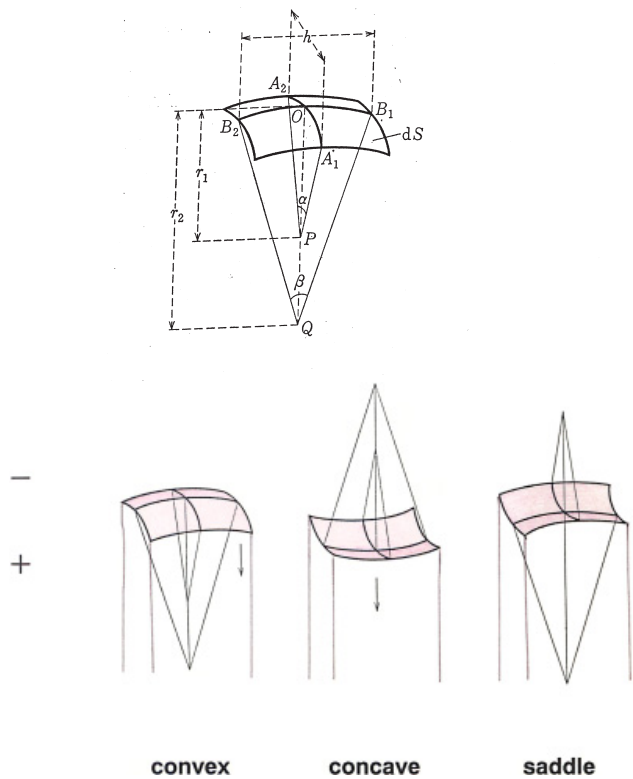

Fig. 7-19. (Upper) The curvature of surface at O is defined by a pair of principal radii r_1 and r_2. (Lower) Three types of surfaces; convex, concave and saddle.

the surviving parenchyma as the structure of interest, which is enveloped by a continuous surface where the three types are considered to be co-existing as small patches assembled in mosaic. Assume as in the upper part of the figure, that we take a point *O* in a small patch of surface convex toward the outside. Then, a pair of principal radii of curvature r_1 and r_2, the minimum and the maximum radii, are defined so that both of the radii extend from *O* along the normal toward the inside of parenchyma. When the surface is cut by a plane that contains the point *O* and the normal, the surface appears on the section as a curve convex toward the outside. In contrast, when *O* is taken at a concave surface as in the center of the lower figure, both of the principal radii of curvature turn out to be extending toward the outside. Here, if the parenchyma is cut with a plane containing one of the principal radii, and then with another plane containing the other, the surface will emerge in each of the sections as a curve concave toward outside. Besides, we have the third type of surface, the saddle surface, as in the right. In this type, one of the principal radii of curvature occurs toward the inside, while the other toward the outside of the parenchymal surface. In reality, in the interphasic membrane of zonal necrosis we are going to study, the saddle parts have the largest share in the total solid angle produced by the interphase (see below). Such being the circumstances, in a 2-D section, we cannot simply regard the convex interphasic curve as being a section of convex surface. Either, the concave curve in section does not always mean that it originates from a concave surface. Thus, it is unavoidable for us to study the matter from a 3-D geometry point of view.

The solid angle ω (Fig. 7-20)

The problem we are going to approach is whether the surface of the parenchymal zone that has survived is convex toward the necrotic zone so uniformly as to make the liver unit definable in the form of Rappaport's acinus.

The surface curvature of the surviving areas can be defined with the solid angle ω, as follows. This is an expansion into 3-D of the 2-D relation which we confirmed to hold between the curvature of an interphasic curve and the angle "subtended" by it (see Figs. 7-3a and 7-3b). In the left part of Fig. 7-20, a circle, *r* in radius, is shown. If

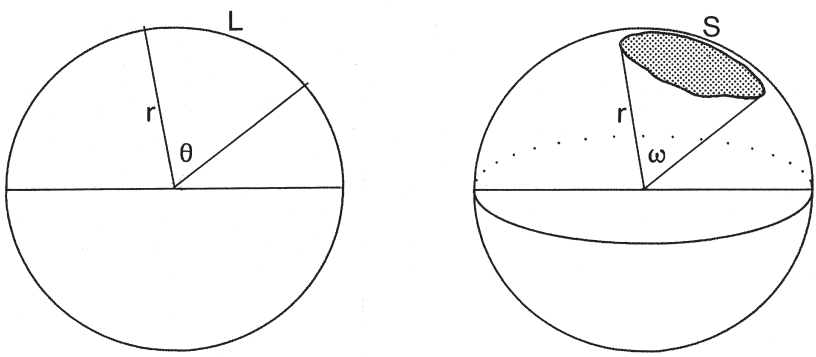

Fig. 7-20. The solid angle.

we take an arc L in length, the curvature of the arc is measured with the angle θ it subtends at the center of the circle. Therefore

$$\theta = L / r .$$

The right part of the figure demonstrates its 3-D counterpart. Here we suppose a sphere of r in radius and a patch of surface on it with an area of S. Also here, the patch makes a curvature corresponding to the solid angle ω it subtends at the center of the sphere. The angle is given, as in the case of 2-D, by

$$\omega = S / r^2 .$$

For a whole sphere, $\omega = 4\pi$ because $S = 4\pi r^2$. Thus the solid angle expresses the spread of space from a point in the form of cone.

Generalization of ω into common surface (Fig. 7-21)

This is generalized into any small patch of surface taken arbitrarily from an object of complicated form. In general, in a minute patch dS arbitrarily cut from a non-spherical surface, for example from a spheroid shown in the left part of Fig. 7-21, the normals erected along the contour do not converge at a point. Still, we can define $d\omega$ by replacing the normals with unitary vectors of the same direction which then are brought so as to converge at a point by parallel translation in the space, as in the right part of Fig. 7-21. The tips of the vectors come to enclose a transformed surface on a sphere, thus defining $d\omega$. This is a process of projecting dS from an arbitrary patch onto a spherical surface.

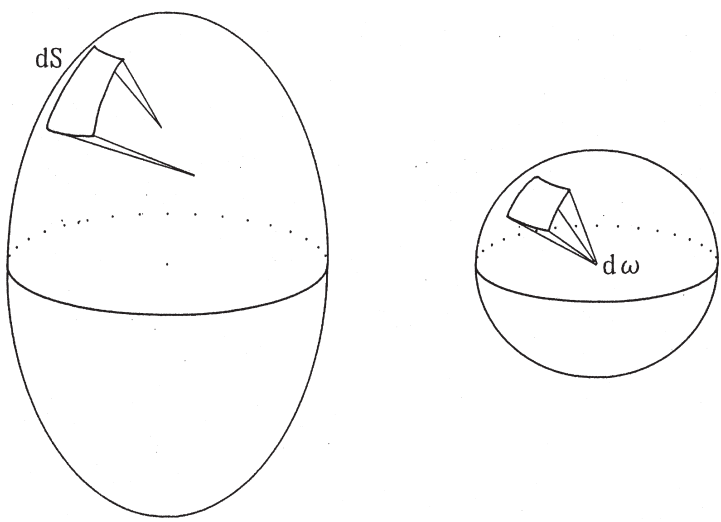

Fig. 7-21. Solid angle of a common surface.

Now we go back to Fig. 7-19 and imagine, as in the upper part of the figure, a small square patch in the surface of parenchymal zone with edges of h in length. If the normal at point O is OQ , we can define the radius of curvature for each of a pair of orthogonal arcs A_1A_2 and B_1B_2, as r_1 and r_2, respectively. It is known that as the arcs are turned around OQ, at the moment when r_1 comes to be the smallest, then r_2 is the largest. In other words, in this situation the curvature k_1 of the arc A_1A_2 is the largest, and k_2 of B_1B_2 is the smallest. The pair of curvatures k_1 and k_2 are called the principal curvatures of the surface at point O. Of course, if the angle subtended by A_1A_2 is α, and that by B_1B_2 is β, then

$$k_1 = \alpha / h$$

$$k_2 = \beta / h .$$

According to principles of solid geometry, we can describe $d\omega$ at an arbitrary point O in terms of Gaussian curvature K, as

$$d\omega = h^2 K,$$

where

$$K = k_1 \, k_2 = 1/ \, r_1 \, r_2.$$

In the definition of Gaussian curvature K, plus and minus rs are to be discriminated. Consider that the radius of curvature r is a vector originating at O. Let r be plus when the vector extends toward the inside of parenchyma, and minus when it extends toward the outside (see Fig. 7-19). Thus, both in convex and concave surfaces, ω is plus because $r_1 \, r_2$ is [++] in the former and [– –] in the latter. In a saddle surface, however, ω is minus on account of the combination [+–].

ω in a constricted surface (Fig. 7-22)

Let us consider in some 3-D surfaces what the solid angle ω amounts to. As shown, ω is $+4\pi$ for a sphere. This holds true not only for a sphere but for any convex bodies like an ellipsoid, where ω is constantly $+4\pi$.

Next, consider a shape of two spheres partially united as in the left part of Fig. 7-22. Because both the upper and lower spherical parts are larger than a hemisphere, ω created by each of the convex parts can be described as $[+2\pi + \alpha]$ and $[+2\pi + \beta]$, respectively ($\alpha > 0$, $\beta > 0$). However, there is a circumferential zone of saddle surface between the two spheres, which produces a minus ω corresponding to $-[\alpha + \beta]$. Consequently, as a whole, $[\alpha + \beta]$ is offset, and we have a total net ω of $+4\pi$. No matter how many spheres are united into a single closed surface, the result is the same, leading to the conclusion that a closed surface of any complicated shape has a net solid angle of $+4\pi$, so long as there is no hole. A saddle surface occurs at places of transition between convexity and concavity, at a constriction, or as in the following, along the margin of hole.

The right part of Fig. 7-22 demonstrates the surface of an open pot. It has an

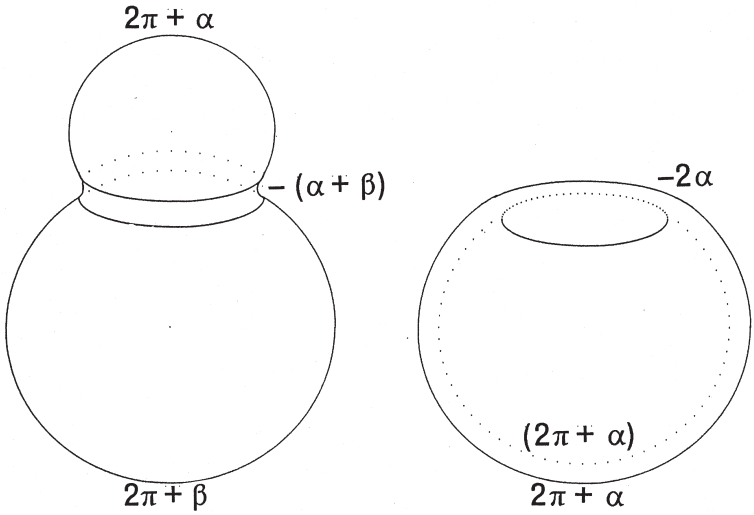

Fig. 7-22. Solid angle of constricted surfaces.

external convex surface which is larger than a hemisphere, with an ω of $2\pi + \alpha$. The internal surface is entirely concave and therefore creates an ω of $2\pi + \alpha$ as well. Along the margin of opening there is a round belt of saddle surface and this creates a negative ω of -2α. Thus, here too, the total ω amounts to $2 \times (2\pi + \alpha) - 2\alpha = +4\pi$, and we find the above conclusion holds true.

ω in a torus: relevance to 3-D topology (Fig. 7-23)

In the next place, let us consider a torus, the surface of a doughnut, as in Fig. 7-23 right. There is a belt of saddle along the inner surface of the hole, generating a negative ω of -4π. It offsets an ω of $+4\pi$ which, if there were no hole, would have been generated by the closed surface.

This will be understood by making a simple ideal experiment. We consider a torus with a circular hole of r in radius, as in the figure. Here suppose that we close the hole by putting a sphere which also has a radius of r. In this situation, ω for the whole body must be $+4\pi$, because there is no longer a hole. Next, assume that we take away the sphere and restore to the original state of torus. The sphere that was separated from the body has an angle of $+4\pi$, and through this procedure no other surface was added or subtracted, which is equivalent to saying that no ω was added or subtracted. Which shows that for the torus, ω is 0 because a solid angle of $+4\pi$ was taken away from a body of $+4\pi$.

Thus, $\omega = 0$ for a torus with one hole. If a surface contains two holes, then the total solid angle amounts to

$$\omega = +4\pi + 2(-4\pi) = -4\pi.$$

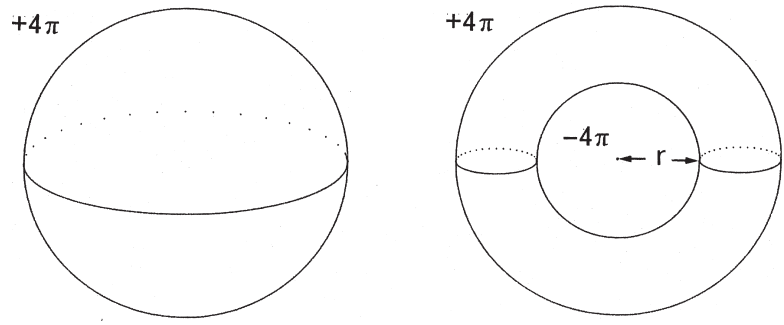

Fig. 7-23. Solid angle of a torus (right).

This can be generalized into

$$\omega = 4\pi(m - c), \tag{7-3}$$

where ω is the total angle generated in the space, m is the number of closed surfaces in the space and c, the number of holes. A closed surface having several holes is nothing but a membrane, or an interface, covering a 3-D network. An example of this sort of surface was already found in cirrhotic livers where the interphase between the nodular and interstitial phases presents as a continuous surface with many holes (see Fig. 6-9). In the above equation, one can see how closely the solid angle generated by surfaces correlates with the connectivity of network the surfaces are covering.

3-D tangent counting by sweeping the space (Figs. 7-24, 7-25)

Here too, we can apply tangent counting method to the estimation of total solid angles contained in a space (DeHoff, 1968). The principle is the same as we have seen in 2-D pictures, where angles "subtended" by linear boundaries were estimated by tangent counting, i.e., sweeping the sample area with a line. In dealing with the problem of curved surfaces, however, sweeping has to be done in the 3-D, requiring to "sweep" by translating a plane through the space. This is a procedure of scanning the space with serial sections. In the schema of Fig. 7-24, we assume that a rectangular space contains surfaces of various shape. Imagine that we slowly move the ceiling ABCD of the space downward by parallel translation, thus sweeping the space. Then the plane comes to touch the surfaces at various points, each time generating a tangent.

Statistically, a tangent occurs at every $+2\pi$ of solid angle at convexity as well as at concavity, while at a saddle, it occurs at an angle of -2π. This may be understood in Fig. 7-25 where, in the left, sweeping of sphere generates two tangents, each corresponding to an angle of $+2\pi$, while in a torus, two tangents add at the saddle, each producing -2π. Therefore if, in a sample space containing a sufficient amount of curving interfaces, we count the number n of tangents and at the same time discriminate among the tangents occurring at convex, concave and saddle surfaces separately, the total ω generated by each of the three different surfaces is given by

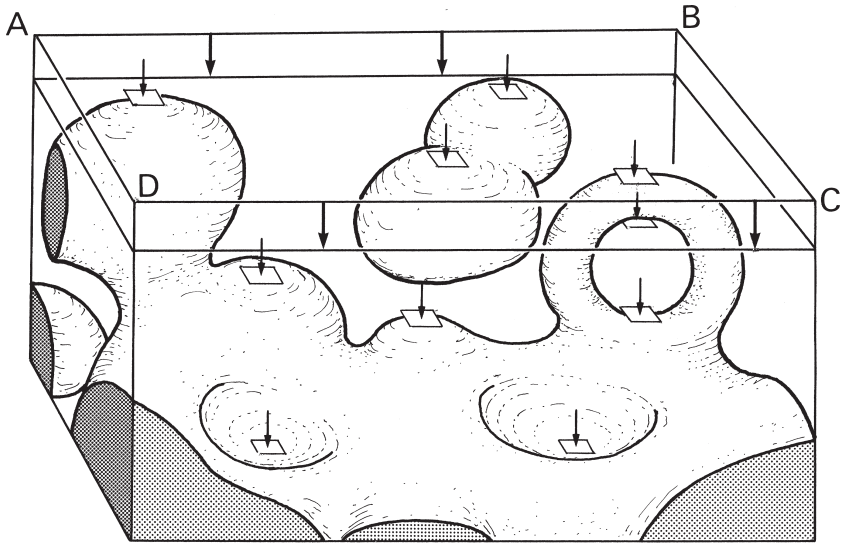

Fig. 7-24. A schema of 3-D tangent counting. Imagine a rectangular space containing surfaces of various shape. Then consider that the ceiling ABCD of the rectangle is moved downward by parallel translation. While moving, the plane comes to touch the surfaces at various points (small arrows), each time generating a tangent. Reproduced from Nakamura and Takahashi: Tohoku J Exp Med (1998) 184: pp. 217.

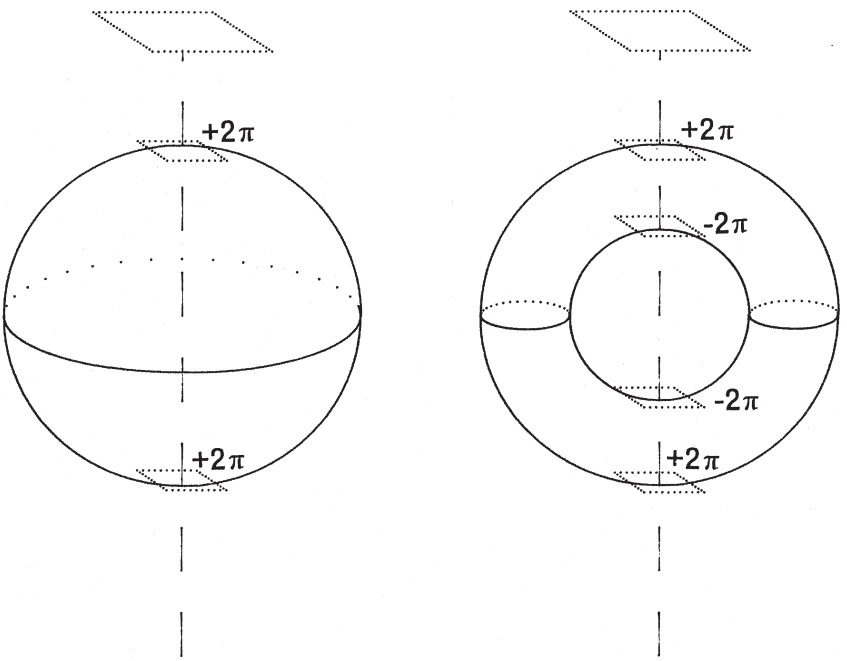

Fig. 7-25. Sweeping: the cases of sphere and torus.

$$\omega\,(\mathrm{cvx}) = +2\pi n(\mathrm{cvx})$$

$$\omega\,(\mathrm{ccv}) = +2\pi n(\mathrm{ccv})$$

$$\omega\,(\mathrm{sdl}) = -2\pi n(\mathrm{sdl})$$

where n(cvx), n(ccv) and n(sdl) denote the number of tangents generated at convex, concave and saddle parts of interface. Thus the total ω contained in the space amounts to

$$\omega = 2\pi\,\{n(\mathrm{cvx}) + n(\mathrm{ccv}) - n(\mathrm{sdl})\}.$$

Tangent counting on serial sections (Fig. 7-26)

Three-D tangent counting by sweeping a sample volume was performed on serial sections of livers with zonal necrosis. As usual, serial 2-D images of the interphasic border between the necrotic and surviving zones were inputted consecutively into a computer, together with the portal and hepatic veins. While scanning the sampled

Fig. 7-26. Counting of 3-D tangents between the test plane and the interphasic surfaces in the liver with hepatocellular necrosis due to cresol intoxication. Counting is performed upon the computer display as 3-D reconstruction advances, as in the figure where the test plane for sweeping is the display itself that is moved in the direction vertical to the section. The green wireframes express the interphasic borders between the necrotic and surviving areas. Red are the portal, and blue are the hepatic veins. Reconstruction was designed so as to progress at a large between-steps interval of 16 μm. In the figure one can recognize several points where a tangent has occurred, for example at A and B. One can recognize that at B, both of the two tangents were generated at a saddle plane. Whether the surface is convex or cancave at a point like A can be determined by observing how the nearby surface changes with the advancement of reconstruction. Reproduced from Nakamura and Takahashi: Tohoku J Exp Med (1998) 184: pp. 227.

volume in a computer display by advancing reconstruction, the places where a tangent occurs could easily be recognized. Whether a tangent arose at a convex, concave or saddle part of interphase was judged by comparing the nearby contour lines, as shown in Fig. 7-26, where a tangent (A) was confirmed arising at convex surface, and two (B) at saddle. Whether the surface like A corresponds to a mountain top or a bottom of depression could be determined by observing what a 3-D form develops in the surroundings as reconstruction progresses.

The result of 3-D tangent counting (Table 7-1)

The result of measurement is listed in Table 7-1. Studied were autopsy livers from five patients. Cases 1 and 2 were selected to represent livers with acute necrosis, both from patients dying of cresol intoxication, 60 and 90 hours after ingestion, respectively. The other three patients had suffered from chronic cardiac failure including cardiac amyloidosis (Case 3), primary pulmonary hypertension with right ventricular failure (Case 4) and aortic regurgitation (Case 5), in all of whom zonal hepatocellular injuries were considered attributable to chronic ischemia and/or congestion. Signs of cardiac failure had lasted 2 years and 8 months (Case 3), 10 months (Case 4) and 4 years and 3 months (Case 5).

Here, the numbers of tangents, n(ccv), n(cvx) and n(sdl), can directly be translated into the share of the corresponding solid angles ω(ccv), ω(cvx) and ω(sdl) in the total solid angle contained in the sampled volume, because, as shown, the value of ω is proportional to the number of tangents. First of all, it is noteworthy that in the acute cases, the share of tangent number at convex surface was only 6% and 3%, while the share at concave surface was as high as 25% and 22%. In contrast, in the chronic cases, this ratio is reversed, with the number of tangents occurring at the convex surface exceeding those at the concave sites. Why, with time, the pattern has changed in such a way may be clear. Within a matter of years, with recurrent bouts of necrosis followed by regeneration of hepatocytes that survivied, the pattern of lesion has gradually come to undergo secondary transformation due to nodular hepatocellular hyperplasia and collapse of necrotic areas. Accordingly, in examining whether the acinar theory can really hold as an anatomical and functional unit, it is crucial to study the

Table 7-1. The result of 3-D tangent counting in 5 livers with zonal hepatocellular injuries.

	Liver weight (g)	Sample volume(mm^3)	Number of tangents n(ccv)	n(cvx)	n(sdl)	ω in sample	Total genus
Acute							
Case 1	1,180	31.0	59(25%)	14(6%)	169(69%)	-192π	1.83×10^6
Case 2	990	17.5	26(22%)	4(3%)	91(75%)	-122π	1.73×10^6
Chronic							
Case 3	830	25.6	16(4%)	89(24%)	222(70%)	-234π	1.90×10^6
Case 4	1,140	29.2	23(4%)	158(27%)	415(70%)	-468π	4.57×10^6
Case 5	946	21.7	23(4%)	136(22%)	467(75%)	-616π	6.71×10^6

pattern of liver lesion fresh from injury. In chronic cases, we find the original shape of injury modified with additional and secondary changes, where the liver has already started advancing toward cirrhosis. In the acute cases of cresol intoxication, there remains no doubt about the shape of parenchyma surviving zonal necrosis. The surviving areas are cast into a shape where the surface concave toward the necrotic zone far exceeds the convex surface. Clearly, this must be quite the opposite to what has been maintained by those supporting the acinar concept.

3-D structure of acute zonal necrosis (Fig. 7-27)

Figure 7-27 presents a 3-D reconstruction of the liver in acute cresol intoxication (Case 1). Clearly, the surface of the surviving parenchyma, presenting as green masses, comprises concave, convex and saddle parts but concavity is likely to be more common than convexity. At no place, necrosis (void) is extending as a sleeve-like flap reaching the portal tract. The parenchymal areas that survived necrosis are only uniformly surrounding the segments of terminal portal veins (pink), without being separated into "acini" demarcated from each other. These are findings least expectable from the acinar model. At several places, one can find connections between adjacent areas of necrosis, disclosing that the overall shape of necrosis, and also that of the surviving parenchyma, are a loose 3-D network.

Thus, the geometry of the interface between the necrotic and surviving phases is a 3-D network. As shown in Chapters 5 and 6, how densely the network is knit can be given by the number of holes (meshes) it contains. This is given by the value of c in

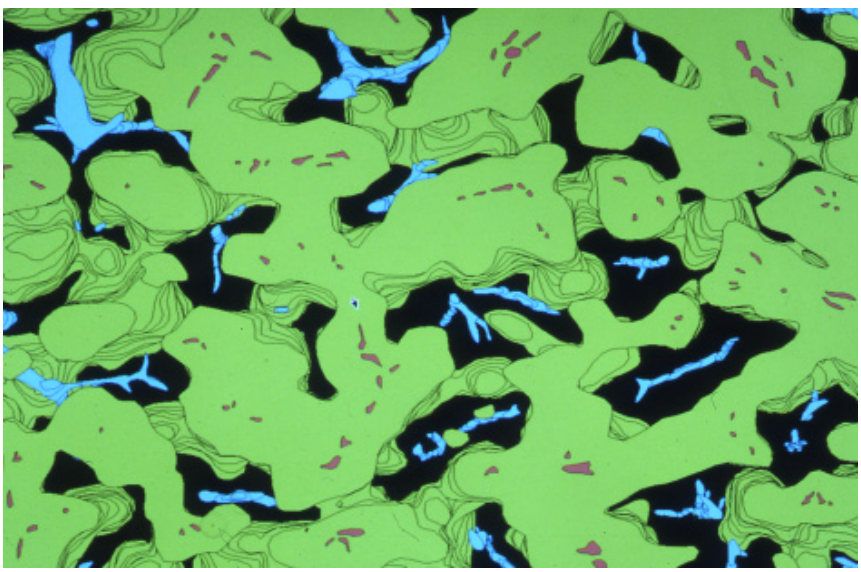

Fig. 7-27. Computer-assisted 3-D reconstruction of the liver with acute injury due to cresol intoxication. The viable parenchyma is painted in green, with the necrotic zones left as void spaces. When viewed from the parenchymal side, the interphasic surface seems mostly to be concave, a situation not compatible with the model proposed in the form of acinar schema. Reproduced from Nakamura and Takahashi: Tohoku J Exp Med (1998) 184: pp. 227.

equation (7-3), which corresponds to the genus given in the descriptions in the foregoing chapter (see Fig. 6-18). Assuming that the specific gravity of the liver is 1.0, the total number of meshes contained in the liver was calculated based on the ratio of the sampling volume to the whole liver. As in Table 7-1, the total number of genus proved to be within a comparatively narrow range from 1.7 to 1.9×10^6 in both of the cresol cases. In the three cases with chronic heart failure, the number was shown comparatively larger in Cases 4 and 5. In Case 5 where the disease lasted as long as four years and 3 months, the network proved to be so dense as to have a genus number of 6.71×10^6. It is interesting that this is a value close to the number of holes in chronic hepatitis, where the total genus number (p_1) was estimated at 6.10×10^6, showing that the two livers share a skeleton that is topologically quite similar (Fig. 6-21). Perhaps there may be some reason for the hepatic microvasculature to deliver a network skeleton of this density, but this belongs to what is to be studied in the future.

After all, the 3-D distribution and shape of acute zonal necrosis turned out to be something quite different from what one would expect to see based on the acinar model. Nowhere "sleeve-like" projection of necrosis was confirmed extending from around the THVs and reaching the portal venule where three terminal portal twigs come to join. The surviving parenchyma was being covered by an interphase where concavity toward necrosis was overwhelmingly predominant over convex surface. All these are not consistent in any respect with the pattern of necrosis which has to be induced from the acinar model.

Then, what a unitary structure of the liver one should assume? Our conclusion is that from a 3-D structure point of view, any unitary concept is not necessary in understanding the structure-function correlation in the liver. We think, the principle of the hepatic microstructure lies in the isodistance between the terminal afferent and efferent vessels, which is realized in the liver in a typical and perfect way compared with other organs.